4-8-2022

Assessment of wettability and rock-fluid interfacial tension of caprock: Implications for hydrogen and carbon dioxide geo-storage

Muhammad Ali

Bin Pan

Nurudeen Yekeen

Sarmad Al-Anssari

Amer Al-Anazi

See next page for additional authors

10.1016/j.ijhydene.2022.02.149

Ali, M., Pan, B., Yekeen, N., Al-Anssari, S., Al-Anazi, A., Keshavarz, A., ... & Hoteit, H. (2022). Assessment of wettability and rock-fluid interfacial tension of caprock: Implications for hydrogen and carbon dioxide geo-storage. International Journal of Hydrogen Energy, 47(30), 14104-14120. https://doi.org/10.1016/j.ijhydene.2022.02.149

Available online at www.sciencedirect.com

ScienceDirect

journal homepage: www.elsevier.com/locate/he

Assessment of wettability and rock-fluid interfacial tension of caprock: Implications for hydrogen and carbon dioxide geo-storage

Muhammad Ali [a,*], *Bin Pan* [b], *Nurudeen Yekeen* [c], *Sarmad Al-Anssari* [d], *Amer Al-Anazi* [a], *Alireza Keshavarz* [e], *Stefan Iglauer* [e], *Hussein Hoteit* [a,**]

[a] *Physical Science and Engineering Division, King Abdullah University of Science and Technology (KAUST), Thuwal, 23955, Saudi Arabia*

[b] *School of Civil and Resource Engineering, University of Science and Technology Beijing, Xueyuan Road, Beijing, China*

[c] *Department of Chemical & Petroleum Engineering, Faculty of Engineering, Technology and Built Environment, UCSI University, 56000, Kuala Lumpur, Malaysia*

[d] *Department of Chemical Engineering, University of Baghdad, Baghdad, 10071, Iraq*

[e] *School of Engineering, Edith Cowan University, Joondalup, WA, 6027, Australia*

HIGHLIGHTS

- The equilibrium contact angle (θ_E) increases with pressure and organic concentration but decreases with temperature.
- The solid-gas interfacial tension (γ_{SG}) decreases with pressure and organic concentration but increases with temperature.
- The solid-liquid interfacial tension (γ_{SL}) and θ_E decreases, whereas γ_{SG} increases with increasing alumina nanofluid concentration.
- Mica hydrogen wettability is less than mica CO_2 wettability in all physio-thermal conditions.

GRAPHICAL ABSTRACT

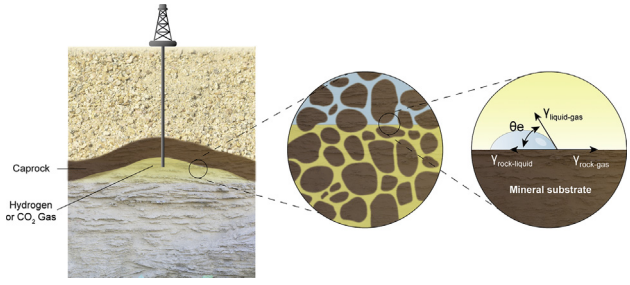

ARTICLE INFO

Article history:
Received 22 October 2021
Received in revised form
13 February 2022

ABSTRACT

Underground hydrogen (H_2) storage (UHS) and carbon dioxide (CO_2) geo-storage (CGS) are prominent methods of meeting global energy needs and enabling a low-carbon global economy. The pore-scale distribution, reservoir-scale storage capacity, and containment security of H_2 and CO_2 are significantly influenced by interfacial properties, including the equilibrium contact angle

* *Corresponding author*. Physical Science and Engineering Division, King Abdullah University of Science and Technology (KAUST), Thuwal, 23955, Saudi Arabia.

** *Corresponding author*. Physical Science and Engineering Division, King Abdullah University of Science and Technology (KAUST), Thuwal, 23955, Saudi Arabia.

E-mail addresses: Muhammad.ali.2@kaust.edu.sa, Muhammad.ali7@postgrad.curtin.edu.au (M. Ali), Hussein.hoteit@kaust.edu.sa (H. Hoteit).

https://doi.org/10.1016/j.ijhydene.2022.02.149

Accepted 17 February 2022
Available online 11 March 2022

Keywords:
Caprock
Hydrogen and carbon dioxide geo-storage
Rock-fluid interfacial tension
Wettability
Organic acids
Alumina nanofluid

(θ_E) and solid-liquid and solid-gas interfacial tensions (γ_{SL} and γ_{SG}). However, due to the technical constraints of experimentally determining these parameters, they are often calculated based on advancing and receding contact angle values. There is a scarcity of θ_E, γ_{SL}, and γ_{SG} data, particularly related to the hydrogen structural sealing potential of caprock, which is unavailable in the literature. Young's equation and Neumann's equation of state were combined in this study to theoretically compute these three parameters (θ_E, γ_{SL}, and γ_{SG}) at reservoir conditions for the H_2 and CO_2 geo-storage potential. Pure mica, organic-aged mica, and alumina nano-aged mica substrates were investigated to explore the conditions for rock wetting phenomena and the sealing potential of caprock. The results reveal that θ_E increases while γ_{SG} decreases with increasing pressure, organic acid concentration, and alkyl chain length. However, γ_{SG} decreases with increasing temperatures for H_2 gas, and vice versa for CO_2. In addition, θ_E and γ_{SL} decrease, whereas γ_{SG} increases with increasing alumina nanofluid concentration from 0.05 to 0.25 wt%. Conversely, θ_E and γ_{SL} increase, whereas γ_{SG} decreases with increasing alumina nanofluid concentration from 0.25 to 0.75 wt%. The hydrogen wettability of mica (a proxy of caprock) was generally less than the CO_2 wettability of mica at similar physio-thermal conditions. The interfacial data reported in this study are crucial for predicting caprock wettability alterations and the resulting structural sealing capacity for UHS and CGS.

Introduction

The rapid industrialization and increasing world population (at a geometrical progression rate) have increased global energy demand and consumption [1]. Fossil fuel has remained the principal global energy source for several decades [2,3], but the world reserve is depleting faster than the discovery rate [4,5]. Moreover, whenever fossil fuels are burned, they release large amounts of greenhouse gases into the atmosphere, contributing to global warming [6–10].

Underground hydrogen (H_2) storage (UHS) and carbon dioxide (CO_2) geo-storage (CGS) have been identified as two effective methods of providing sufficient global energy needs and creating a low-carbon global economy by reducing carbon emissions [11–15]. The primary aims of UHS and CGS are substituting fossil fuel with decarbonized and clean fuels (H_2) [14,16,17], converting excess renewable energy into H_2 through electrolysis [14,18], and capturing CO_2 from stationary sources or the atmosphere and sequestering it in geologic formations [19–21]. In addition, CO_2 sequestration involves the permanent and secure storage of the captured gas in underground formations. In contrast, UHS involves the storage of H_2 in geo-storage locations (such as depleted oil and gas reservoirs, coal seams, deep saline aquifers, and organic-rich shales) and its withdrawal at the period of peak demand [14,16,17,22–24].

However, the success of UHS and CGS is greatly influenced by several thermo-physical and petro-physical factors [18]: the wettability of the rock-brine-gas systems and the interfacial tension (IFT) between the rock and fluids (i.e., gases or brine) [25,26]. These crucial parameters govern the fluid distribution in the reservoir, the injection of CO_2 and H_2 into the reservoir, and the subsequent H_2 withdrawal [27–32]. Evaluation of the rock wetting phenomenon and rock-fluid IFT is crucial to assess the gas storage capabilities of the storage-rock and caprock formations. It also provides operational constraints to avoid leakage hazards and ensure containment safety at realistic storage conditions [27,33–35].

Generally, reasonable efforts have been invested in measuring the contact angle of rock-brine-CO_2 systems in previous studies [25,36–38]. However, only four studies have reported contact angle datasets for rock-brine-H_2 systems [26,34,39,40]. Measuring the contact angle of rock-brine-H_2 systems is challenging due to high H_2 reactivity, volatility, compressibility, and metal embrittlement [34,41].

The possibility of industrial-scale H_2 storage in sandstone reservoirs (mainly consisting of quartz) with the presence of organic acid contamination was investigated by Iglauer et al. [31] and Ali et al. [34]. Iglauer et al. [31] demonstrated that higher contact angles were measured at an elevated temperature and pressure with the presence of a minute concentration of organic acid. The results from Ali et al. [34] agreed with those from Iglauer et al. [31], confirming that the intrinsically strongly water-wet clean quartz substrate became H_2-wet (the advancing contact angle increased from 40.8° to 91.3°) when aged in lignoceric acid (10^{-2} M) at 25 MPa and 323 K. Similarly, Ali et al. [26] found that pure mica substrates became intermediate-wet at higher pressures and lower temperatures, whereas organic acids converted them into H_2-wet.

In contrast, for rock-fluid IFT, only gas-brine IFT ($\gamma_{gas-brine}$) can be conveniently measured in the laboratory [27]. Rock-gas IFT data (γ_{rock-H_2} and $\gamma_{rock-CO_2}$) are scarce in the literature, as these parameters cannot be determined by experimental estimations [27,42,43]. For rock-brine-CO_2 systems, researchers computed these data theoretically through the combination of Neumann's equation of state and Young's Laplace equation [27,29,30,42–47]. Arif et al. [43] found that mica-CO_2 IFT ($\gamma_{mica-CO_2}$) was higher at high temperatures and lower at high pressures. Similarly, Pan et al. [46] demonstrated that $\gamma_{quartz-CO_2}$ is considerably lower than $\gamma_{quartz-CH_4}$ at similar thermo-physical conditions.

To the best of our knowledge, only Pan et al. [27] computed rock-fluid IFT for rock-brine-H_2 systems using a semi-empirical technique, suggesting that evaluating rock-fluid IFT data for rock-H_2-brine systems at geo-storage conditions requires further investigation. Pan et al. [27] reported that the values of rock-gas IFT were smaller at a higher temperature and elevated pressure and were reduced with an increased organic acid concentration. However, the reported rock-fluid IFT data were primarily for quartz, a representative mineral in a sandstone formation. Thus far, no data are available for rock-fluid IFT for caprock representative minerals (i.e., mica). Hence, the associated structural trapping capacities of the caprock during H_2 and CO_2 storage conditions are still unknown, which motivated this work.

Initially, the advancing (θ_a) and receding (θ_r) contact angles of the mica-H_2-brine and mica–CO_2–brine systems were measured for pure, organic-aged, and nano-aged substrates. Afterward, we computed the mica-fluid IFT data (γ_{mica-H_2}, $\gamma_{mica-CO_2}$, and $\gamma_{mica-brine}$) using the combination of Young's equation and Neumann's equation of state in geo-storage conditions.

The focus has been on investigating the influence of temperature, pressure, gas type (CO_2 and H_2), organic acid concentration, alkyl chain length, and nanofluid concentration on contact angles and rock-fluid IFT data in mica-H_2-brine and mica–CO_2–brine systems. To our knowledge, this study provides the first reported rock-fluid IFT data for H_2 and a caprock representative mineral (mica) at subsurface conditions. The data indicate favorable conditions for effective structural trapping capacities of the caprock and gas containment security during UHS and CGS.

Materials and methods

Materials

The details of the materials used for this study are presented in Tables 1 and 2, where mica (muscovite) is used as a representative mineral for the caprock. The contact angle measurements for H_2 and CO_2 were conducted with a 10 wt% NaCl aqueous solution at reservoir conditions. Four types of organic acids with varying carbon chain lengths (lignoceric acid C_{24}, stearic acid C_{18}, lauric acid C_{12}, and hexanoic acid C_6) were used as representative organic molecules in geological formations to age the mica substrates [35,48–51] (Table 2). The mica samples were cleaned with ultra-pure nitrogen before aging to eliminate impurities from the mica surface. The various organic acid concentrations were prepared using n-decane as the base solution. The mica substrate surfaces were cleaned with methanol, acetone, and toluene (99.9 mol % pure, Rowe Scientific). Hydrophilic aluminum oxide (Al_2O_3) nanoparticles were used to improve the wetting phenomenon of organic-aged mica substrates.

Table 1 – Materials used for this research.

Materials	Suppliers	Other details
Pristine mica	Ward's natural science	L x W x H = 20 × 15 × 3 mm
NaCl	Chemlab	≥99.9 mol % purity
Deionized water	David Gray	0.02 mS/cm electrical conductivity
N-decane	Chem-supply	99.9 mol % pure
Nitrogen	BOC	99.999 wt% ultra-pure (gas code 234)
CO_2	BOC	99.999 wt% ultra-pure (gas code 082)
H_2	BOC	99.999 wt% ultra-pure (gas code 240)
Hydrochloric acid	Sigma Aldrich	>99% pure, 37.5% concentration
Hydrophilic aluminum oxide (Al_2O_3) nanoparticles	Sigma Aldrich	Particle size (13 nm), surface area (85–115 m^2/g), purity (≥99.8 wt%)

Cleaning and aging procedure for mica substrates with organic acids

Pure mica substrates must be cleaned because they contain impurities in the initial condition that could influence the experimental results. Therefore, mica substrates were first cleaned with deionized water, and then the samples were blown with ultra-clean nitrogen and dried at 353 K for 30 min to eliminate the thin water film. Afterward, the residual minute organic impurities were removed by treating the mica samples with air plasma (Diemer Yocto instrument) for 20 min [35,52,53].

Realistic caprock conditions were replicated through the following process. First, mica surfaces were inserted into brine (2 wt% NaCl) for half an hour at room conditions to ionize the surface. A pH of 4 in the brine solution was maintained by adding HCl droplets. This procedure promotes the adsorption of the organic acid on the mica surfaces to mimic realistic geological conditions [35,49,51,54].

Subsequently, ultra-pure nitrogen flow was used to remove the residual brine from the modified mica surfaces. Then, the HCl-brine ionized substrates were put in diverse solutions of n-decane or organic acid mixtures, with concentrations of 10^{-2}, 10^{-3}, 10^{-5}, 10^{-7}, and 10^{-9} mol/L. The mica surfaces were aged in organic solutions for 1 week to imitate exposure to formation water for prolonged geological stints [35,49,51,54]. Next, mica substrates were cleaned with ultra-pure nitrogen followed by drying for 24 h at 343 K to remove any excessive organic or n-decane solution before contact angle measurements. The mica substrates became hydrophobic after aging in the organic solutions because of the chemisorption of organic acids on the mica surfaces [35,55].

Mica substrate characterization

Measurement of the total organic carbon

The total organic carbon (TOC) of the aged and unaged mica substrates was measured using the pyrolysis method with the Rock-Eval 6 instrument (Vinci Technologies) [35]. The TOC of the clean mica substrates was insignificant (around 500 ppm due to air contamination). However, when the mica substrate was aged in organic acids, the TOC increased up to 1800 ppm owing to organic acid chemisorption. The TOC results

Table 2 – Organic acid details.

Name	Formula	Molecular mass (g/mol)	Number of carbon atoms	pH (pKa)	Physical state	Chemical structure
Lignoceric acid	$C_{24}H_{48}O_2$	368.63	24	7.4	Solid	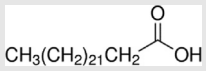
Stearic acid	$C_{18}H_{36}O_2$	284.4772	18	6	Solid	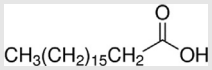
Lauric acid	$C_{12}H_{24}O_2$	200.318	12	5.3	Solid	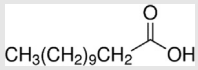
Hexanoic acid	$C_6H_{12}O_2$	116.158	6	4	Liquid	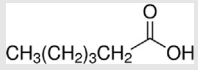

presented in Fig. 1 are responsible for altering the wetting characteristics of the mica substrates.

Surface characterization of mica substrates

Energy dispersive spectroscopy coupled with a field-emission scanning electron microscope (SEM; Oxford Instruments) and atomic force microscopy (Nanosurf, Flex-Axiom, and Controller C3000) were used to analyze the elemental composition and surface topography of the clean and aged mica substrates. The pure mica surfaces were very smooth, and their surface roughness was 1–2 nm. Moreover, organic acid adsorption has very little effect on the surface roughness (and, thus, the contact angle), and the root mean square ranges from 200 to 460 nm. Many wettability studies have reported that a surface roughness of less than 1 μm does not significantly influence the contact angle measurements [56–58].

The SEM micrographs of the mica substrate before and after aging in stearic acid (10^{-2} mol/L concentration) are presented in Fig. 2, exhibiting a uniform coverage of the organic acid on the mica surface. A significant increase in the carbon concentration on the mica surface was observed for the aged mica substrates. For instance, the mean carbon content of the pure mica increased from 3.2 ± 0.5 to 5.0 ± 1.6 wt% when aged in lignoceric acid solution, from 3.2 ± 0.6 to 4.8 ± 1.6 wt% when aged in stearic acid solution, from 3.1 ± 0.7 to 4.4 ± 1.7 wt% when aged in lauric acid solution, and from 2.9 ± 0.7 to 3.9 ± 0.8 wt% when aged in hexanoic acid solution (Table 3, the total energy dispersive spectroscopy values of each mica organic added substrate is depicted in the supplementary file in Table S1). These results can be attributed to the organic acid chemisorption on mica surfaces [34].

Preparation of the alumina nanofluid

Different nano-alumina concentrations (0.05–0.75 wt%) were prepared using the sonication technique to explore their capacity to alter the wetting phenomenon of the mica–CO_2–brine system. The desired Al_2O_3 nanoparticle concentrations were dispersed in ionized water using a magnetic stirrer to ensure homogeneity. Afterward, the solutions were sonicated using an ultrasonic homogenizer (Sonics and Materials Incorporation, USA) for 15 min at a frequency of 20 kHz with 40% sonication amplitude and an energy of 9500 J [59].

Determination of nanofluid stability

The stability of the prepared nanofluids dispersions must be ascertained because agglomerations of nanoparticles in deionized water or brines (associated with nanoparticle hydrophobicity and surface energy) could decrease the wettability reversal properties [50,60,61]. The stability and phase behaviors were estimated from the hydrodynamic particle sizes and zeta-potential values measured using a Malvern nano zeta-sizer (Model: ZS ZEN 3600) at pH conditions representative of deep saline aquifers (6–12 pH) [62]. A greater absolute zeta-potential value (>30 mV) suggests that repulsive forces are dominant among nanoparticles, whereas a lower absolute zeta-potential value (i.e., near the isoelectric point, which is 0 mV) represents the dominancy of attractive forces among nanoparticles. These greater attractive forces result in a greater agglomeration and sedimentation ability of nanoparticles. Generally, greater agglomeration is observed when particles are exposed to a saline environment [63–65].

The zeta potential and hydrodynamic particle size at different pH values are presented in Table 4. The data indicate that nano-alumina has zero isoelectric points in deionized water (when the pH values range from 8 to 10). The zeta potential decreased, whereas the average particle size increased with the increasing concentration of nanoparticles. Table 4 further suggests that the alumina nanofluids are promising candidates for reversing the wettability of the mica-gas-brine system into more hydrophilic conditions due to the wide range of zeta-potential values (48 to −40 mV) [59]. Specifically, low nanoparticle agglomeration (158 and 206 nm) and higher

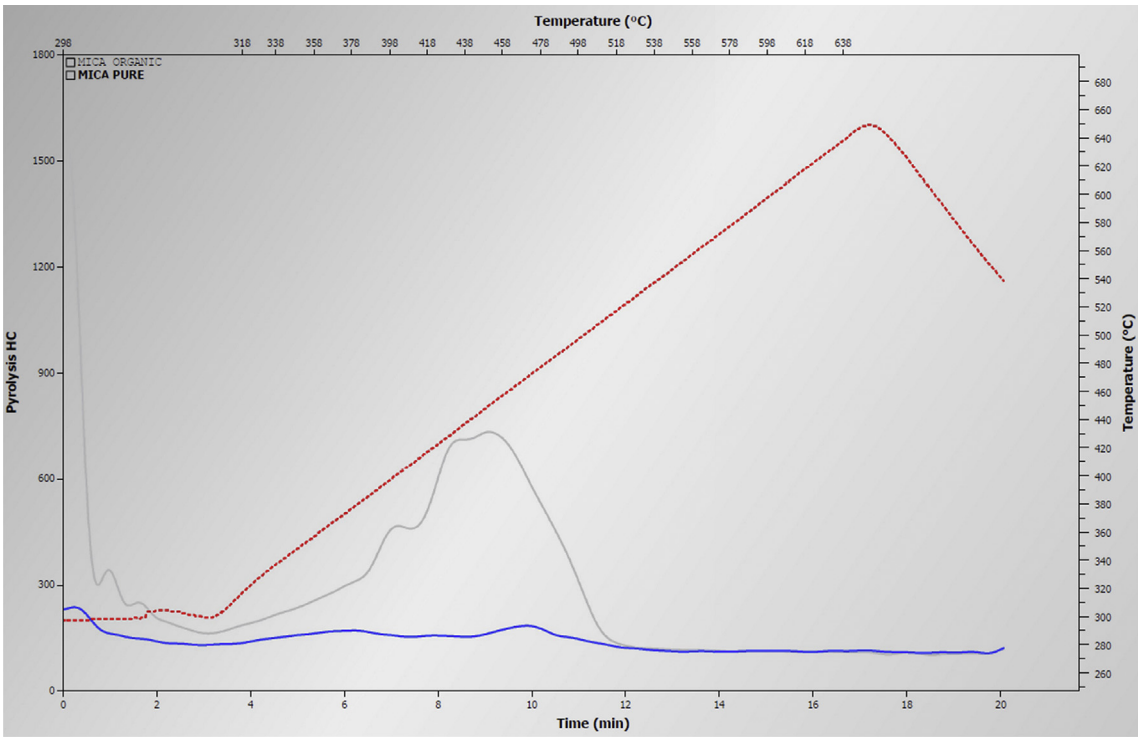

Fig. 1 – Total organic carbon (TOC) of the aged and unaged mica substrate. The blue line represents mica, and the gray line indicates organic aged mica. (For interpretation of the references to color in this figure legend, the reader is referred to the Web version of this article.)

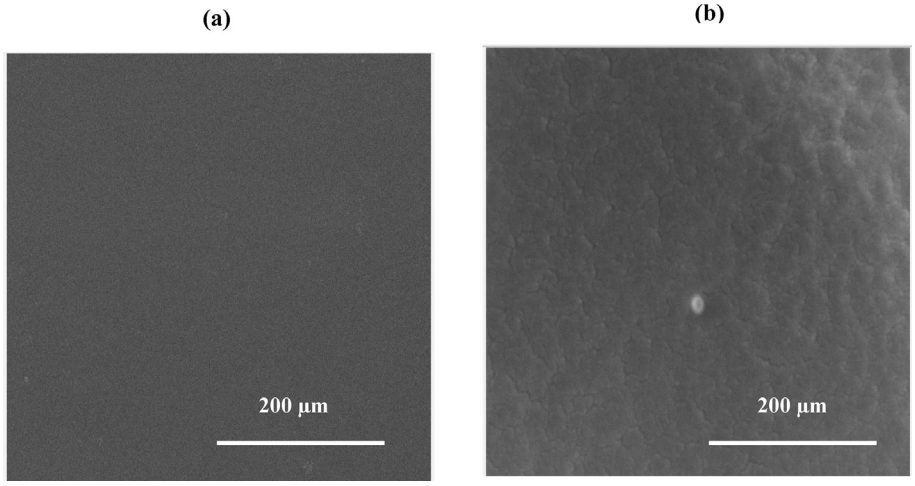

Fig. 2 – Scanning electron micrographs of (a) a clean mica surface and (b) a mica surface aged in stearic acid/n-decane solution at 10^{-2} mol/L concentration.

Table 3 – Mean elemental values of pure and aged mica substrates.

Organic acids	After aging					Before aging				
	Si (wt%)	C (wt%)	O (wt%)	Al (wt%)	K (wt%)	Si (wt%)	C (wt%)	O (wt%)	Al (wt%)	K (wt%)
Lignoceric acid	20.6 ± 1.1	5.0 ± 1.6	47.8 ± 1.8	19.0 ± 1.0	7.7 ± 1.0	22.5 ± 1.0	3.2 ± 0.5	46.4 ± 1.5	19.2 ± 1.1	8.8 ± 0.7
Stearic acid	20.8 ± 1.3	4.8 ± 1.6	48.1 ± 1.7	19.2 ± 1.0	7.2 ± 0.9	22.3 ± 1.2	3.2 ± 0.6	46.1 ± 0.9	19.7 ± 0.8	8.7 ± 0.7
Lauric acid	21.0 ± 1.3	4.4 ± 1.7	48.2 ± 2.0	18.9 ± 1.0	7.6 ± 0.7	22.2 ± 0.9	3.1 ± 0.7	46.8 ± 2.0	19.6 ± 0.9	8.3 ± 0.7
Hexanoic acid	20.0 ± 1.4	3.9 ± 0.8	50.3 ± 2.8	18.5 ± 1.3	7.4 ± 1.1	21.8 ± 1.7	2.9 ± 0.7	48.2 ± 2.1	19.2 ± 0.8	7.9 ± 0.5

Table 4 – Zeta potential and hydrodynamic particle size of alumina nanofluid concentrations at different pH values.

pH	Zeta potential (mV)				Average particle size (nm)			
	0.05 wt%	0.1 wt%	0.25 wt%	0.75 wt%	0.05 wt%	0.1 wt%	0.25 wt%	0.75 wt%
6	48.35	48.35	46.5	40.6	158	158	167	207.5
8	17.62	16.85	11.545	10.305	551.6	540	494.4	525
10	−6.13	−10.65	−14.35	−18	1056	642.5	512.5	540
12	−28.4	−29.46	−38.8	−39.75	206	202	192.5	235.9

stability (48.35 and −28.4 mV) is noticed at 6 and 12 pH for a 0.05 wt% nanofluid concentration, whereas a higher agglomeration (551.6 and 1056 nm) and lower stability (17.62 and −6.13 nm) is noticed at pH values of 8 and 10 for a 0.05 wt% nanofluid concentration. A similar trend was also observed for other nanofluid concentrations. Thus, the irreversible adsorption of the alumina nanofluid on the mica surface occurred through the definite interaction of −OH ions with the positive charges of the mica substrates [59].

Aging process of organic-aged mica in alumina nanofluid

The mica substrates (aged in organic acid or n-decane solutions) were vertically immersed in different concentrations of nano-alumina formulations (0.05–0.75 wt%) for 5 h at 323 K and ambient pressure. The samples were submerged perpendicularly to minimize gravitational settling of nano-alumina at the ratio of 5:1; that is, for every 5 g of nanofluid dispersion, 1 g of mica was used. The nanoparticles were permanently adsorbed onto the mica surface due to the chemical reaction or interaction of the positively charged hydroxyl group of mica substrate with the negatively charged hydroxyl group of nanofluid dispersions.

This phenomenon altered the wettability of the initially hydrophobic mica surfaces (originally aged in organic acid or n-decane) to an intermediate-wetting state when aged in alumina nanofluids. Generally, organic acid or n-decane mica surfaces became CO_2-wet due to the esterification of the substrates with organic acids via a condensation reaction. However, the Al_2O_3 nanoparticles were irreversibly adsorbed on the aged mica to restore the original wettability state before the organic acid adsorption [50,55,59].

Measurements of the contact angle of mica-H_2-brine and mica–CO_2–brine systems

Advancing (θ_a) and receding (θ_r) contact angles of the rock-gas-brine systems were measured at reservoir conditions (5, 10, 15, and 20 MPa and 308 K, 323 K, 343 K for pure mica and 15 and 25 MPa and 323 K for organic- and nano-aged mica) using the tilted plate method (17° tilted angle) [50]. A detailed description of the equipment and procedure for the contact angle measurements with their sources and types was described in our previous studies [26,35,59]. Initially, the mica substrates (pure, organic-aged, and nano-aged) were inserted into the sample holder (at 17° tilted arrangement), and the cell was firmly closed. Then, H_2 or CO_2 was gradually injected to reach the desired temperature (308 K–343 K) and pressure (0.1–25 MPa). After the cell was filled with H_2 or CO_2 at the desired operating temperature and pressure, equilibrated brine droplets (5 ± 0.75 μL) were introduced onto the tilted mica surface with a high-precision pointer. Subsequently, θ_a and θ_r were filmed at the trailing and leading edges of the droplet with a high-performance video camera [35]. The contact angles on the images were measured with image analysis software (Image J). For every experimental condition, measurements were replicated thrice, and the mean values of θ_a and θ_r were computed [66]. The standard deviation of the experiments at 0.1–15 MPa was ±3°, whereas that of experiments at 20–25 MPa was ±5°.

Computation of the solid-fluid interfacial tension and equilibrium contact angle

Comprehensive procedures for calculating the solid-fluid IFT have been reported in the literature [27,43–47]. In addition, the relevant computation procedure is provided concisely in this section.

As the equilibrium contact angle (θ_E) at thermodynamic equilibrium conditions is not accessible by experiment [67], the below equation calculates θ_E:

$$\theta_E = \arccos\left(\frac{\varkappa_A \cos\theta_A + \varkappa_R \cos\theta_R}{\varkappa_A + \varkappa_R}\right) \quad (1)$$

where θ_A and θ_R represent experimental advancing and receding brine contact angles:

$$\varkappa_A = \left(\frac{\sin^3\theta_A}{2 - 3\cos\theta_A + \cos^3\theta_A}\right)^{\frac{1}{3}} \text{ and } \varkappa_r = \left(\frac{\sin^3\theta_R}{2 - 3\cos\theta_R + \cos^3\theta_R}\right)^{\frac{1}{3}} \quad (2)$$

Combining Young's equation (Eq. (3)) and Neumann's equations of state (Eqs. (4) and (5))

$$\cos\theta_E = \frac{\gamma_{SG} - \gamma_{SL}}{\gamma_{LG}} \quad (3)$$

$$\gamma_{SG} = \gamma_{SL} + \gamma_{LG} - 2\sqrt{\gamma_{SL}\gamma_{LG}}\left[1 - \beta(\gamma_{SL} - \gamma_{LG})^2\right] \quad (4)$$

$$\gamma_{SL} = \gamma_{SG} + \gamma_{LG} - 2\sqrt{\gamma_{SG}\gamma_{LG}}\left[1 - \beta(\gamma_{SG} - \gamma_{LG})^2\right] \quad (5)$$

obtains Eq. (6), as follows:

$$\cos\theta_E = 1 - 2\sqrt{\frac{\gamma_{SL}}{\gamma_{LG}}}\left[1 - \beta(\gamma_{SL} - \gamma_{LG})^2\right] \quad (6)$$

where γ_{SG}, γ_{SL}, and γ_{LG} are the solid-gas, solid-liquid, and liquid-gas IFTs, respectively, and β is the adjustable constant [27].

Further, in Eq. (6), θ_E and γ_{LG} are input parameters, and the γ_{LG} data at various pressures and temperatures were collected from Ref. [68], as presented in Figure S1 (supplementary file), and β are the fitting parameters. Further, to mimic in situ gas geo-storage scenarios, the brine was not saturated with any

gas prior to γ_{LG} measurements, and finally, γ_{SG} was determined using Eq. (4).

Results and discussion

Effect of temperature and pressure on equilibrium contact angles and rock-fluid IFT of pure mica-gas-brine systems

As a low-permeability clay mineral, mica can represent a proxy of caprock, and its wettability has a great influence on the structural sealing potential during gas geo-storage [26,35]. The geo-storage formation temperature and pressure change with depth [69]; thus, we investigated the effects of temperature and pressure on the equilibrium brine contact angle (θ_E), rock-gas IFT (γ_{SG}), and rock-brine IFT (γ_{SL}) for pure mica-gas-brine systems, as illustrated in Figs. 3–5.

Equilibrium contact angle of the pure mica-gas-brine system

The effects of temperature and pressure on the equilibrium brine contact angle (θ_E) of the pure mica-gas-brine system were investigated and presented in Fig. 3. Clearly, θ_E increased with increased pressure and decreased temperature. For example, in the UHS scenario (i.e., the gas is H_2), θ_E increased from 20° to 47° as the pressure increased from 5 to 20 MPa at 323 K, and θ_E increased from 19° to 41° when the temperature reduced from 343 K to 308 K at 10 MPa. In the CGS scenario (i.e., the gas is CO2), θ_E rose from 32° to 79° with rising pressure from 5 to 20 MPa at 323 K, and θ_E increased from 47° to 62° once the temperature reduced from 343 K to 308 K at 10 MPa,

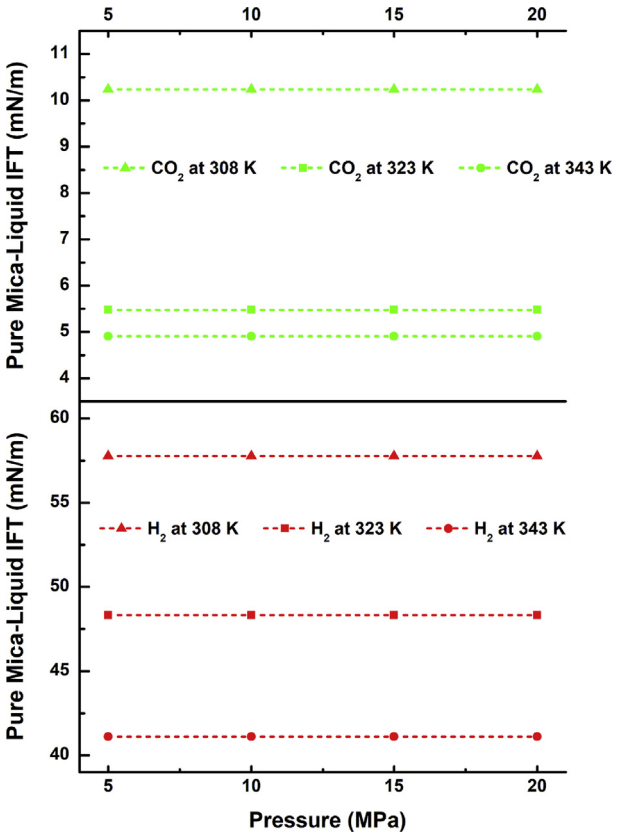

Fig. 4 – Effect of pressure and temperature on the pure mica-brine interfacial tension (IFT).

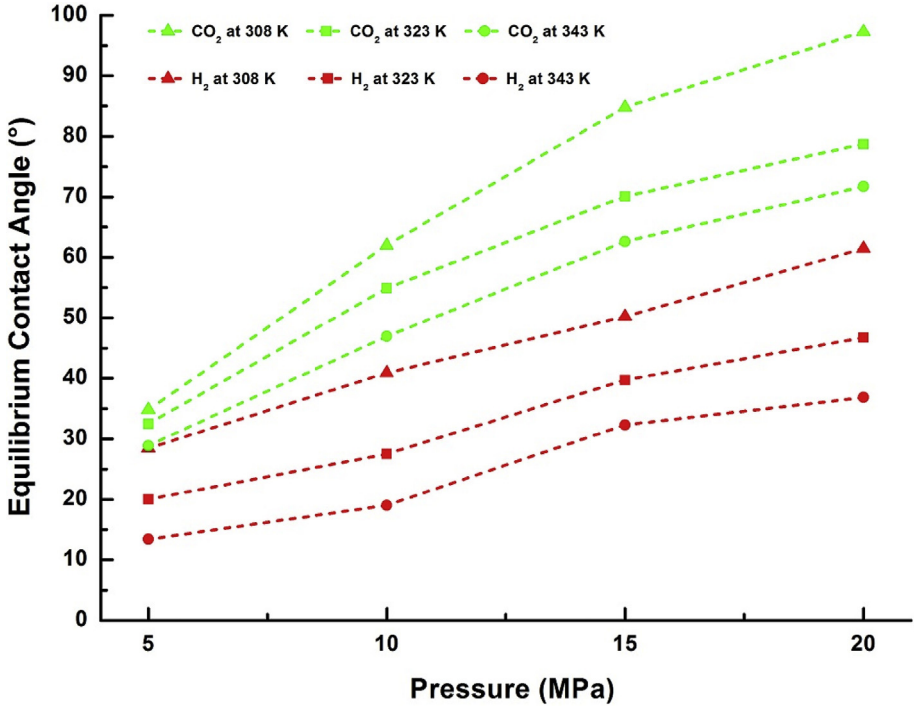

Fig. 3 – Effect of pressure and temperature on the equilibrium brine contact angle of a pure mica-gas-brine system. Readers are referred to Ref. [26] for advancing and receding contact angle data regarding pure mica-H_2-brine and to Ref. [75] for pure mica–CO_2–brine.

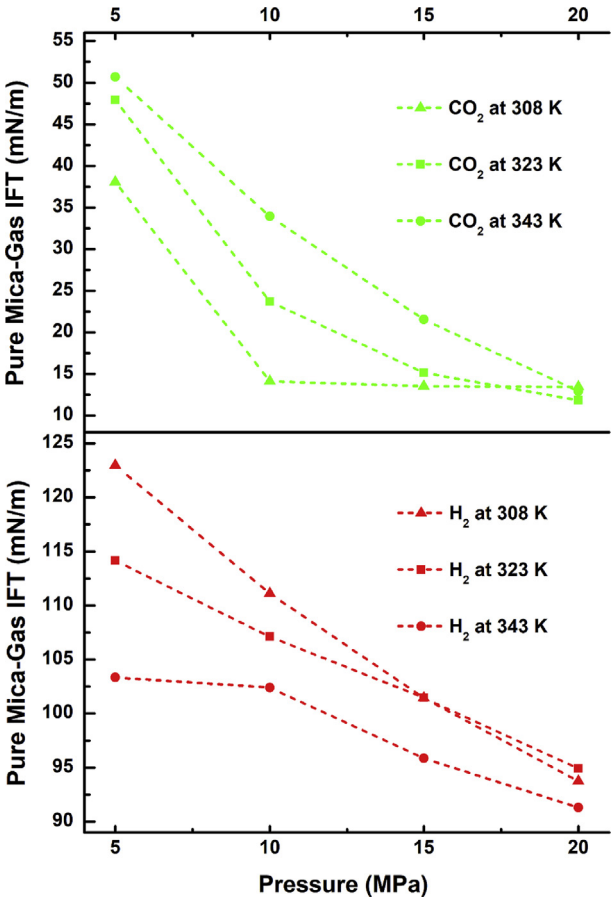

Fig. 5 – Effect of pressure and temperature on the pure mica-gas interfacial tension (IFT).

indicating that mica wettability shifted from intermediate-wet to weakly water-wet [8,70].

Fundamentally, pressure effects on the wettability (contact angle) are attributed to the intermolecular force and gas density [69,71,72], whereas the effect of the temperature on wettability (contact angle) is due to the intermolecular force and interfacial energy [73]. Generally, CO_2 and H_2 densities increased with increased pressure and decreased temperature [25]. Consequently, the intermolecular interaction between the gases and solid (rock surface) is higher at high pressures and lower at high temperatures [25,74].

According to the Young-Laplace equation, a larger contact angle leads to smaller capillary forces [76,77]. Thus, the gas structural trapping capacity could be reduced, resulting in a higher risk of gas leakage [78]. Thus, the formation temperature and pressure (i.e., depth) effects must be considered regarding the structural storage capability and containment safety for UHS and CGS projects [78]. However, at the same thermo-physical conditions, θ_E for H_2 was always lower than θ_E for CO_2. For example, at 20 MPa and 343 K, the θ_E values for H_2 and CO_2 were 37° and 72°, respectively because H_2 has a smaller gas density than CO_2; thus, weaker intermolecular forces exist between H_2 and the mica surface compared to CO_2 and the mica surface [71,79].

Pure mica-brine interfacial tension

Brine density is almost constant at various pressures [25,80], resulting in a weak dependency of the intermolecular forces between the mica and brine on pressure (Fig. 4). The mica-brine IFT (γ_{SL}) remained constant as the pressure increased from 5 to 20 MPa. However, γ_{SL} is sensitive to temperature change because increasing temperatures reduce the liquid density, as the energetic brine molecules occupy more space upward. For example, for H_2, γ_{SL} reduced from 58 to 41 mN/m as the temperature rose from 308 K to 343 K. For CO_2, raising the temperature from 308 K to 343 K dropped γ_{SL} from 10 to 5 mN/m. Likewise, γ_{SL} for H_2 was much larger than that for CO_2.

Pure mica-gas interfacial tension

The pure mica-gas IFT (γ_{SG}) decreased with increasing pressure for both gases, as depicted in Fig. 5. For instance, at 323 K, by raising the pressure from 5 to 20 MPa, γ_{SG} for H_2 dropped by 19 mN/m (from 114 to 95 mN/m), and γ_{SG} for CO_2 reduced by 36 mN/m (from 48 to 12 mN/m). These results are qualitatively consistent with the pressure influence on basalt-gas and quartz-gas IFT values [27,46].

In contrast, the effect of temperature on γ_{SG} depends on the gas type. Specifically, at 10 MPa, γ_{SG} for H_2 reduced by 9 mN/m (111–102 mN/m), whereas γ_{SG} for CO_2 increased by 20 mN/m (14–34 mN/m), as the temperature was elevated from 308 K to 343 K.

The decreasing mica-gas IFT with increasing pressure can be ascribed to the adhesion of the CO_2 or H_2 onto mica surfaces due to the increasing cohesive energy density of H_2 or CO_2, resulting in favorable mica-gas interactions enhancing the mica-H_2 or mica-CO_2 wettability [43]. Fig. 5 further confirms that γ_{SG} for H_2 was larger than γ_{SG} for CO_2 at similar thermo-physical conditions because of fewer van der Waals interactions between the mica substrates and H_2 molecules with lower density compared to CO_2 [43]. For instance, at 343 K and 15 MPa, the γ_{SG} values for H_2 and CO_2 were computed as 96 and 22 mN/m, respectively.

In principle, for a particular gas type, the rock-gas intermolecular forces and gas density increase with increasing pressure [71,79]; thus, γ_{SG} reduces correspondingly [46]. For several gas types, at a similar temperature and pressure state, the density of CO_2 is higher than that of H_2. Consequently, γ_{SG} follows the opposite order: γ_{SG} for H_2 is larger than γ_{SG} for CO_2. This finding is qualitatively harmonious with the latest reported results on the influence of gas density on basalt-CO_2, shale-CO_2, and quartz-H_2 IFT values [27,29,30]. In contrast, a lower γ_{SG} represents higher contact angles (and, thus, hydrophobic wettability), which represents lower gas storage capacities (e.g., $\theta > 90°$ may cause structural leakage) [49,54].

Effect of organic acids, alkyl chain length, and pressure on equilibrium contact angles and rock-fluid IFT of organic-aged mica-gas-brine systems

As organic matter adsorption and contamination prevail in the subsurface (e.g., deep saline aquifers or depleted hydrocarbon reservoirs) [81–84], the influence of organic matter adsorption on the interfacial properties of caprock at reservoir

conditions must be explored. Therefore, in this section, the effects of the concentrations and types of organic acid (as a model organic matter) on the interfacial characteristics of mica were investigated (Figs. 6–8).

Equilibrium contact angle of the organic-aged mica-gas-brine system

The equilibrium brine contact angle (θ_E) of the organic-acid-adsorbed mica-gas-brine system decreased with the decreasing concentration and carbon number of organic acid at constant thermos-physical conditions (Fig. 6). For instance, at a constant pressure (25 MPa) and temperature (323 K) representative of CGS conditions, as the concentration of stearic acid increased from 10^{-9} to 10^{-2} mol/L, θ_E increased from 74° to 117°, indicating that the mica wettability shifted from intermediate-wet to weakly CO_2-wet [70]. Similarly, at the same thermo-physical UHS conditions, θ_E increased from 60° to 95°, indicating that the mica wettability shifted from weakly water-wet to intermediate-wet [26]. With a constant pressure of 25 MPa, the organic acid concentration (10^{-5}mol/L) and increasing carbon number (6–24, i.e., from hexanoic to lignoceric acid), θ_E increased from 78° to 99° for mica–CO_2–brine systems. Likewise, a similar trend was observed regarding the influence of organic acid concentration and carbon number on θ_E under UHS conditions, where θ_E increased from 65° to 84°, as depicted in Fig. 6.

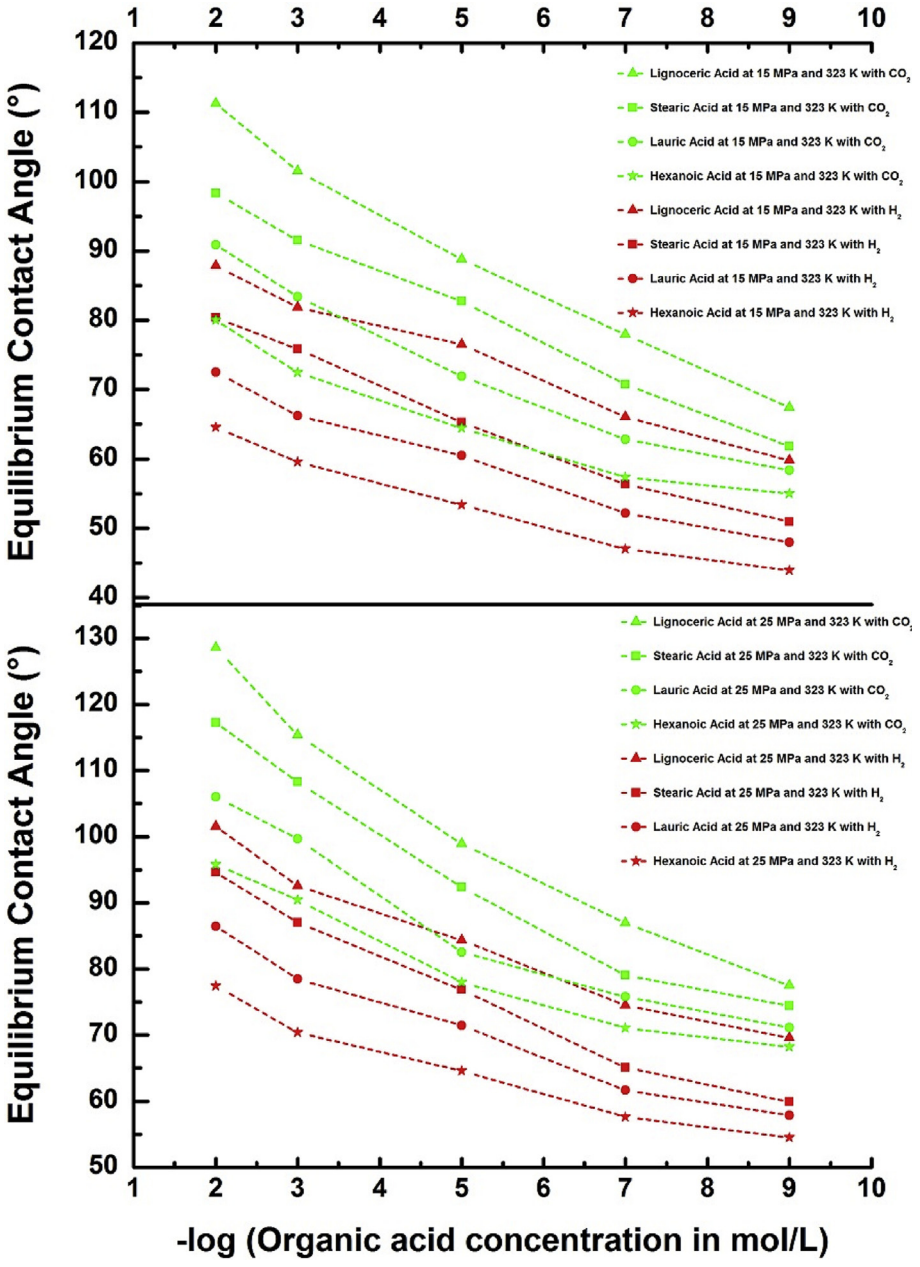

Fig. 6 – Effect of pressure and various organic acid concentrations on the equilibrium contact angle of the mica-gas-brine system. Readers are referred to Refs. [26,85] for advancing and receding contact angle data for organic-aged mica-H_2-brine and to Ref. [35] for organic-aged mica–CO_2–brine.

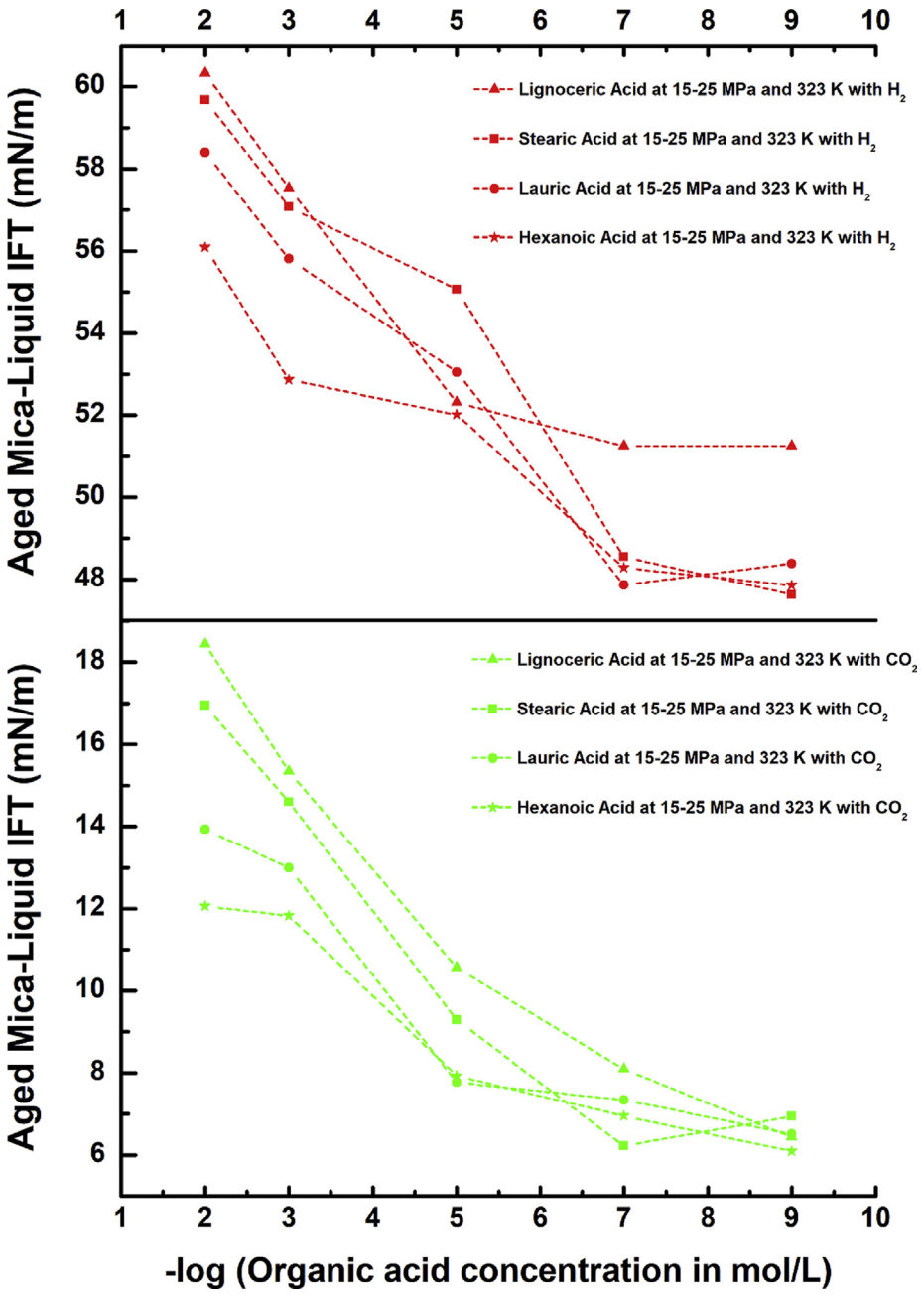

Fig. 7 – Effect of pressure and various organic acid concentrations on the mica-brine interfacial tension (IFT).

Increasing the concentration of organic acid and the carbon number resulted in stronger adsorption of organic acid molecules on mica surfaces [86]. Such strong adsorption of organic acid on the substrate surface and a high organic acid molecular coverage can significantly modify the wetting condition of the surface toward a less hydrophilic state [49,51,53,54,87,88]. A strong repulsion of polar H_2O molecules occurs from the hydrophobic surface, whereas the nonpolar H_2 and CO_2 approach the hydrophobic surface more easily and are easily attached to the mica surface. Thus, the response of the observed θ_E to the organic concentration and carbon number in Fig. 6 can be reasonably explained.

Organic-aged mica-brine interfacial tension

The results reveal that the brine density does not affect the mica-brine IFT (γ_{SL}) with the increase in pressure (Fig. 7). However, when the concentration of the organic acid and carbon number increased, the adsorbed organic acid (γ_{SL}) also increased, as depicted in Fig. 7. Specifically, under UHS conditions (at 15–25 MPa and 323 K), with the increasing lignoceric acid concentration from 10^{-9} to 10^{-2} mol/L, γ_{SL} rose from 51 to 60 mN/m. Similarly, at the same thermo-physical CGS conditions, γ_{SL} rose from 6 to 18 mN/m, when the lignoceric acid concentration increased from 10^{-9} to 10^{-2} mol/L. Whereas, at 15–25 MPa and 323 K, the constant organic acid concentration

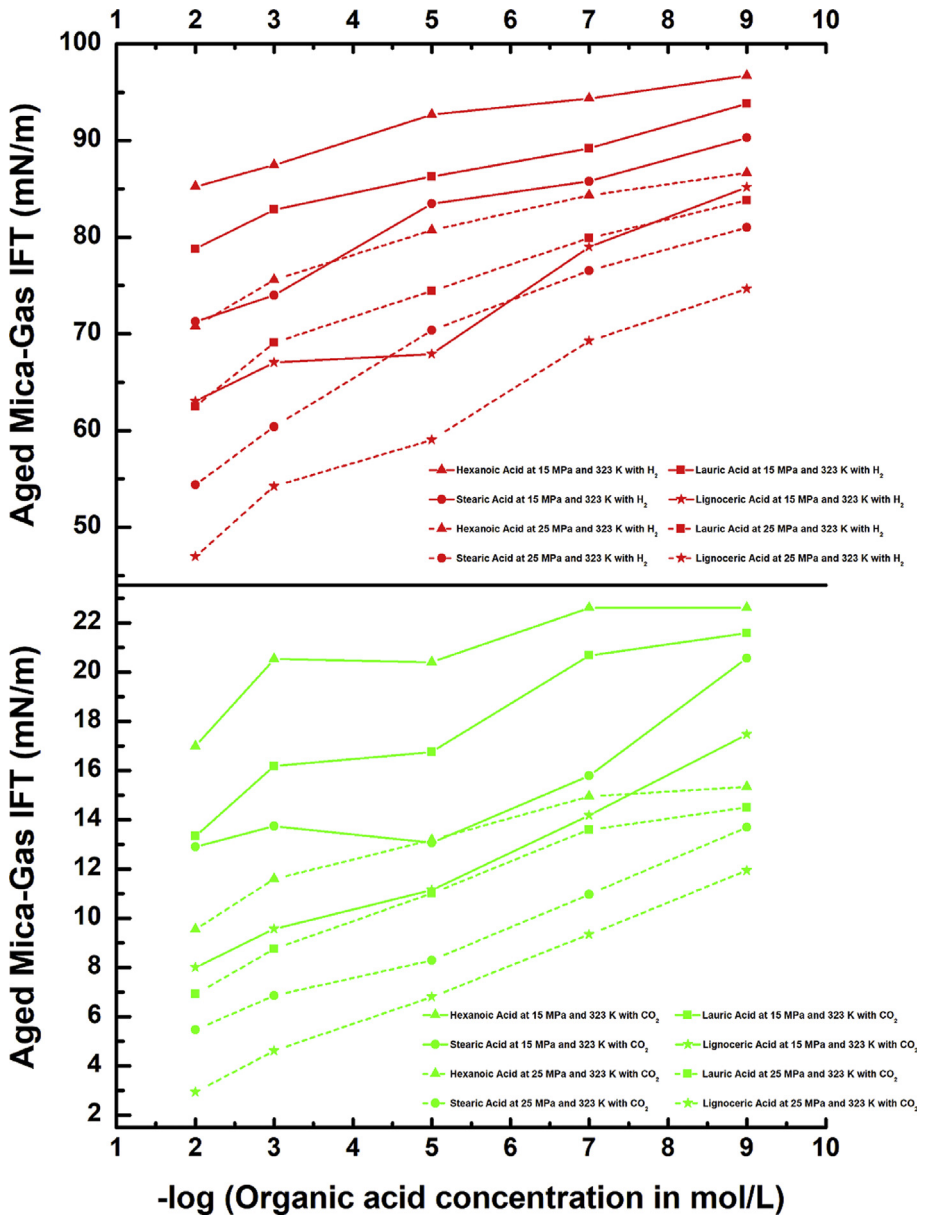

Fig. 8 – Effect of pressure and various organic acid concentrations on the mica-gas interfacial tension (IFT).

(10^{-3}mol/L) and increasing carbon number (6–24, i.e., from hexanoic to lignoceric acid), γ_{SL} increased from 53 to 58 mN/m for mica-H_2-brine systems. Likewise, a similar trend was observed regarding the influence of the organic acid concentration and carbon number on γ_{SL} under the same CGS conditions, where γ_{SL} increased from 12 to 15 mN/m, as depicted in Fig. 7. These results prove that the extent of organic matter adsorption is a crucial factor influencing the rock-fluid IFT.

In line with the mechanism of organic acid adsorption influence on the equilibrium contact angle, stronger organic acid adsorption (induced by a greater concentration of organic acid and carbon number) causes a higher energy barrier for spreading water on aged mica substrate. Consequently, γ_{SL} values were higher with a higher carbon number and an increasing organic acid concentration because the surfaces become less water-wet when the IFT between the mica and brine is higher [43].

Organic-aged mica-gas interfacial tension

The mica-gas IFT (γ_{SG}) decreased with an increasing concentration of organic acid and carbon number, as depicted in Fig. 8. For example, at 323 K and 25 MPa, under UHS conditions, γ_{SG} dropped to 62 from 84 mN/m with the increasing concentration of lauric acid from 10^{-9} to 10^{-2} mol/L. Similarly, at the same thermo-physical CGS conditions, γ_{SG} dropped to 7 from 15 mN/m with the increasing concentration of lauric acid from 10^{-9} to 10^{-2} mol/L. Whereas, at 25 MPa and 323 K, the constant organic acid concentration (10^{-2}mol/L) and increasing carbon number (6–24, i.e., from hexanoic to lignoceric acid), γ_{SG} reduced from 10 to 3 mN/m for mica–CO_2–brine systems.

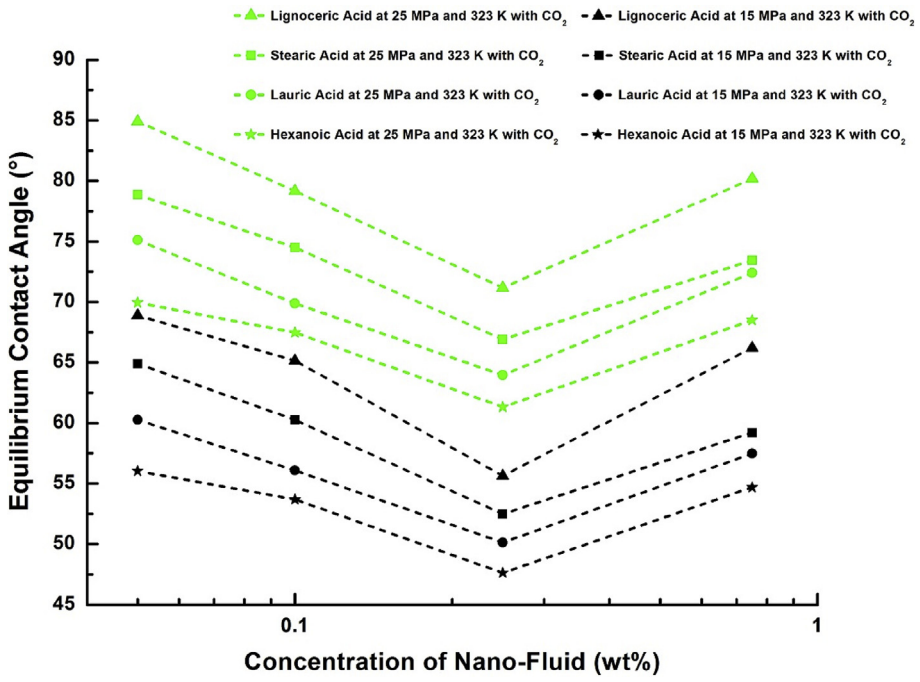

Fig. 9 – Effect of pressure and various alumina nanofluid concentrations on the equilibrium contact angle of the mica–CO_2–brine system. Readers are referred to Ref. [59] for advancing and receding contact angle data regarding alumina aged mica–CO_2–brine.

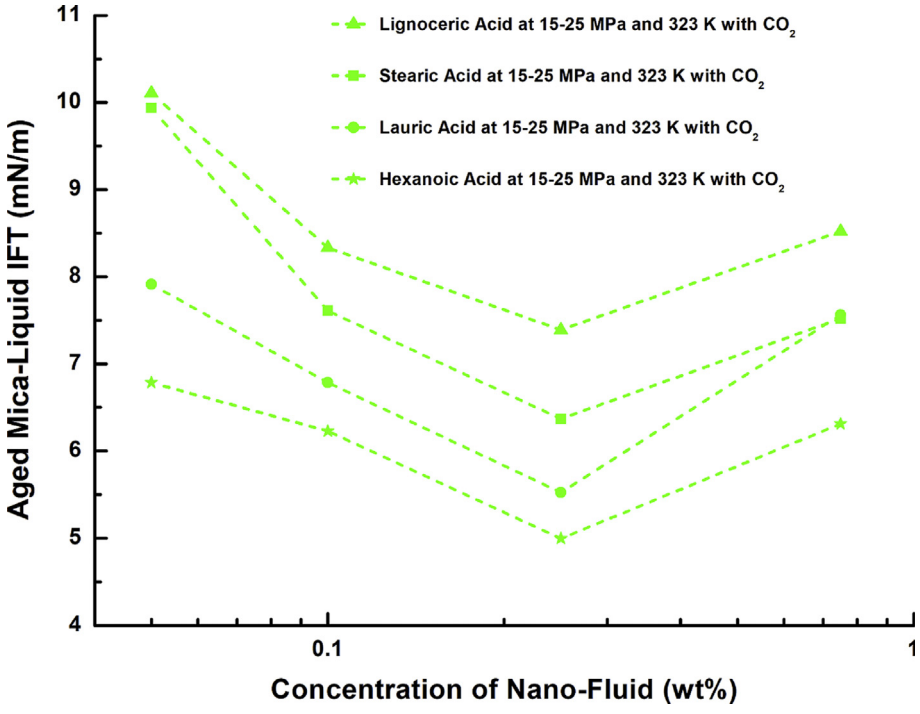

Fig. 10 – Effect of pressure and various alumina nanofluid concentrations on the mica-brine interfacial tension (IFT).

Likewise, a similar trend was observed regarding the influence of the organic acid concentration and carbon number on γ_{SG} under the same UHS conditions, where γ_{SG} dropped to 47 from 71 mN/m, as depicted in Fig. 8. This is because stronger organic acid adsorption causes a lower energy barrier for gas molecules to approach the mica surface.

Influence of the alumina nanofluid concentration and pressure on equilibrium contact angles and the rock-fluid IFT of the nano-aged mica–CO_2–brine system

Nanofluids are widely used for various subsurface applications, including altering the wettability of a gas-wet system into a water-wet system [59,63,64,89,90] and modifying the interfacial properties of hydrophobic caprock [50,55,91]. Threshold concentrations of nanofluids are crucial, where wetting characteristics and interfacial properties of caprock can be improved to implement CGS projects successfully. Therefore, this section presents the investigation of the effect of various concentrations of alumina nanofluid on the interfacial and wetting characteristics of the mica–CO_2–brine system (Figs. 9–11).

Equilibrium contact angle of the alumina aged mica–CO_2–brine system

Generally, θ_E decreased initially with an increasing alumina nanofluid (Al_2O_3) concentration (Fig. 9), but θ_E later increased with an increasing nanofluid concentration, which occurs when the optimum concentration threshold is passed [50,59]. At realistic CGS conditions, the mica caprock was first aged in various organic acids (at a concentration of 10^{-2} mol/L) to build an initial baseline. Then, the organic-aged mica surfaces were aged in different concentrations of alumina nanofluid

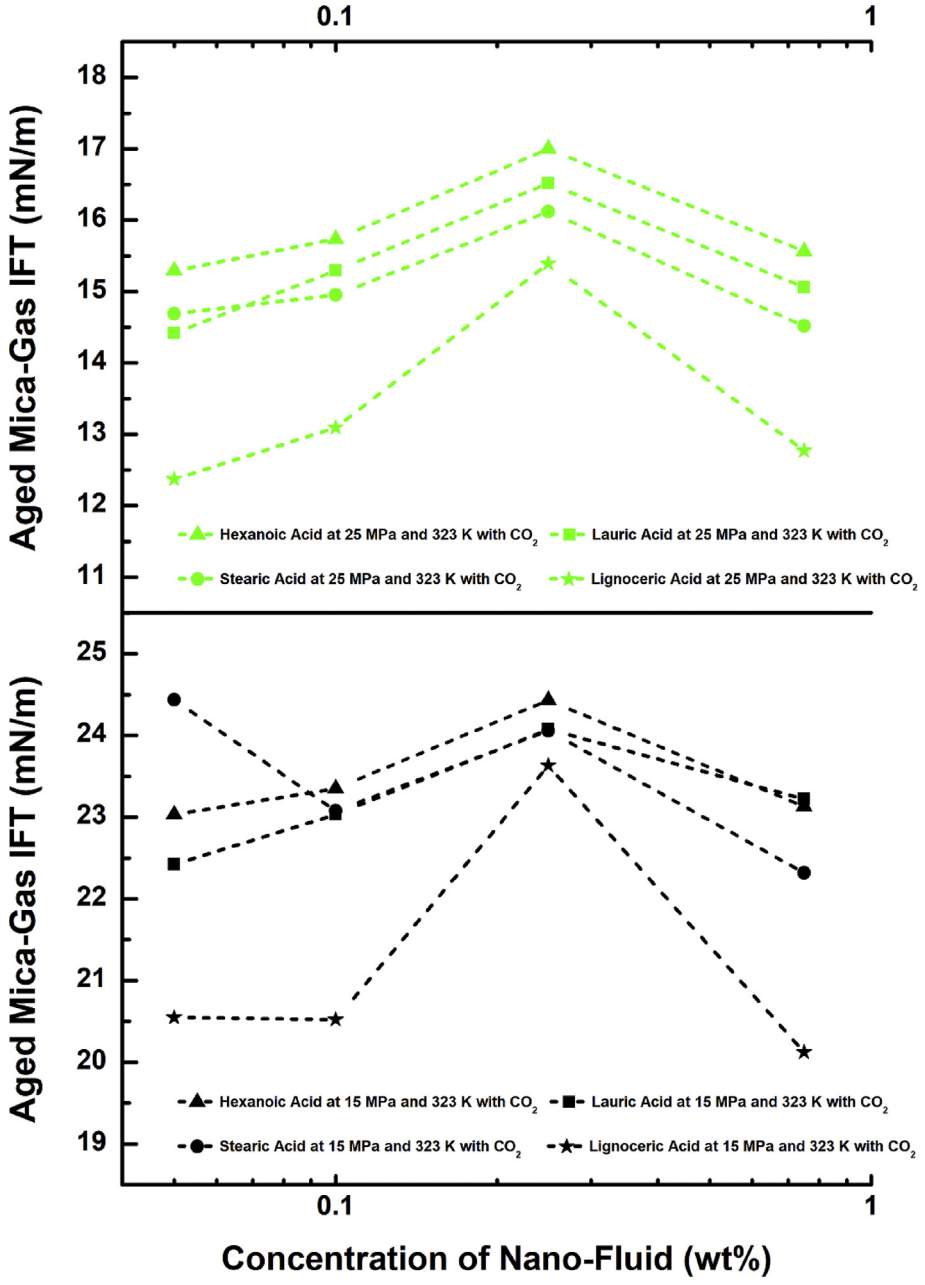

Fig. 11 – Effect of pressure and various alumina nanofluid concentrations on the mica-CO_2 interfacial tension (IFT).

(0.05, 0.1, 0.25, and 0.75 wt%). At 25 MPa and 323 K with lignoceric aged mica substrates, θ_E decreased from 85° to 71° with an increasing Al_2O_3 concentration from 0.05 to 0.25 wt%, but as the Al_2O_3 nanofluid concentration further increased from 0.25 to 0.75 wt%, θ_E increased from 71° to 80°, as depicted in Fig. 9.

These results suggest that 0.25 wt% of alumina nanofluid is the optimum nanoparticle concentration ensuring a significant reduction in the contact angle. The principal mechanism for the modification of the mica surface wettability (reduction in contact angle , θ_E) when aged in alumina nanofluid is ascribed to the permanent adsorption of Al_2O_3 nanoparticles onto the surface of mica [50,59]. Precisely, Al_2O_3 nanoparticles adsorbed evenly on the surface of the aged mica substrate as the concentration increased from 0.05 to 0.25 wt%. The existence of −OH charges on nano-alumina dispersions plays a prominent role in ensuring the success of the irreversible adsorption of Al_2O_3 nanoparticles onto the positively charged mica surface (with the −OH group presence) [59], attracting water molecules to the nano-alumina treated surface, whereas CO_2 is repelled from the mica surface. This phenomenon is similar to the reported alteration of the negatively charged quartz surface wettability by nano-silica (with negative charges) and has been identified as a critical reason for the alteration of hydrophobic into hydrophilic surfaces when aged in nanofluids [27,50,55,92].

However, the agglomeration of nanoparticles, resulting in the increased surface roughness of mica substrates, may occur at certain nanoparticle concentrations (0.75 wt% or upward). Cassie-Baxter's model revealed that the attraction of water to surfaces reduces when the surface roughness of such water-wet surfaces increases [27,93,94]. Hence, θ_E increased as the nanofluid concentration increased from 0.25 to 0.75 wt% because higher energy is required to adhere water molecules to the surface compared to gas molecules [27]. Moreover, at higher nanofluid concentrations, the agglomerated particles reside in the bulk solution instead of irreversibly adsorbing onto mica surfaces, hindering the migration of surface-active species.

Alumina nanofluid aged mica-brine interfacial tension

Consistent with the literature study on the effect of silica nanofluid for quartz-brine IFT [27], the mica-brine IFT (γ_{SL}) also decreased as the initial alumina nanofluid concentration increased and then increased with the further increase in alumina nanofluid concentration (Fig. 10). For example, for the lignoceric acid aged mica, at 15−25 MPa and 323 K, γ_{SL} reduced from 10 to 7 mN/m as the Al_2O_3 nanofluid concentration rose from 0.05 to 0.25 wt%, suggesting that the attraction and spread of water on the mica surface become favorable at the optimum nanofluid concentration.

However, γ_{SL} increased from 7 to 9 mN/m with the further increase in the Al_2O_3 nanofluid concentration from 0.25 to 0.75 wt%, suggesting that the CO_2 wettability of mica became more favorable (gas molecules are more attracted to the mica surface), whereas the surface became less water-wet.

Alumina nanofluid aged mica-CO_2 interfacial tension

In comparison, the mica-gas IFT (γ_{SG}) increased with the increase in the initial alumina nanofluid (Al_2O_3) concentration, whereas γ_{SG} decreased again with the further increase in the Al_2O_3 nanofluid concentration (Fig. 11). For example, at 15 MPa and 323 K with the lauric acid aged mica surface, γ_{SG} increased from 22.4 to 24.1 mN/m with the rising concentration of Al_2O_3 nanofluid (0.05−0.25 wt%), whereas γ_{SG} reduced from 24.1 to 23.2 mN/m with a further increase in the Al_2O_3 nanofluid concentration from 0.25 to 0.75 wt%. The γ_{SG} datasets confirmed the results from the equilibrium contact angle and γ_{SL} that an optimum nano-alumina concentration exists for altering mica substrates contaminated with organic acids inherent in geo-storage formations into less hydrophobic conditions. These nanofluid concentration thresholds should be determined to assess storage-rock and caprock sealing potentials successfully and avoid containment uncertainties during UHS and CGS projects.

Conclusion

The wetting characteristics and rock-interfacial properties (including θ_E, γ_{SL}, and γ_{SG}) of caprock at reservoir conditions are essential parameters that govern fluid distribution during the injection and storage of CO_2 and H_2 in storage rock and caprock and the subsequent withdrawal of H_2 at the peak demand period [49,51,70,75,78,95−98]. However, due to the technical constraints of measuring these three parameters through laboratory experiments, the rock-fluid interfacial data, particularly related to the H_2 sealing potential of caprocks, are rarely reported in the literature [27]. Consequently, we calculated these three parameters for CO_2 and H_2 geo-storage conditions. Moreover, the influences of the concentration and carbon number of organic acid and nanofluids were explored to ascertain the extent of wetting phenomenon modifications by organic contamination inherent in geo-storage formations and the tendency of Al_2O_3 nanofluids to restore the original wetting state.

The following conclusions are drawn from this study:

1. The θ_E increases with increasing pressure, increasing the concentration of organic acid and carbon number but decreases with increasing temperature, suggesting that high pressure and the existence of organic contamination are unfavorable for CO_2 and H_2 storage. In contrast, warmer reservoirs could be ideal storage sites.
2. The γ_{SG} reduces with increasing values of pressure, organic acid concentration, and carbon number, confirming that the adhesion and spread of water molecules to the rock surface are minimal, whereas the gas molecules wet the mica surfaces at high pressure and in the presence of organic acids with a high carbon number.
3. Further, θ_E, γ_{SL}, and γ_{SG} do not demonstrate a monotonous relationship with the Al_2O_3 nanofluid concentration as θ_E and γ_{SL} decrease, whereas γ_{SG} increases with an increasing nano-alumina concentration from 0.05 to 0.25 wt%. Conversely, θ_E and γ_{SL} increase, whereas γ_{SG} decreases with an increasing nano-alumina concentration from 0.25 to 0.75 wt%, implying that the optimum Al_2O_3 nanofluid concentration (0.25 wt%) is essential for improving the sealing potential of the caprock.
4. Higher contact angles and lower solid-gas IFT were obtained for mica−CO_2−brine systems compared to mica-H_2-brine

systems at all investigated conditions, indicating that the H_2 wettability of caprock is always less than the CO_2 wettability of caprock at similar thermo-physical conditions.

This study provides critical insight into the structural UHS and CGS trapping capacities of caprock and the associated containment safety. Further, the work also guides subsurface modifications to optimize gas geo-storage conditions. This study presents the first documented rock-fluid IFT data for caprock representative minerals regarding UHS in downhole conditions. These data aid in the correct prediction of the structural sealing potential of caprock and suggest the conditions for modifications of the rock wetting phenomenon during UHS and CGS projects.

Declaration of competing interest

The authors declare that they have no known competing financial interests or personal relationships that could have appeared to influence the work reported in this paper.

Acknowledgments

The authors acknowledge Mr. Antonio García, a scientific illustrator from King Abdullah University of Science and Technology, Saudi Arabia, for producing the graphical abstract.

Appendix A. Supplementary data

Supplementary data to this article can be found online at https://doi.org/10.1016/j.ijhydene.2022.02.149.

REFERENCES

[1] Mohanty US, Ali M, Azhar MR, Al-Yaseri A, Keshavarz A, Iglauer S. Current advances in syngas (CO+ H2) production through bi-reforming of methane using various catalysts: a review. Int J Hydrogen Energy 2021;46(65):32809–45.
[2] Perera F. Pollution from fossil-fuel combustion is the leading environmental threat to global pediatric health and equity: solutions exist. Int J Environ Res Publ Health 2018;15:16.
[3] Nazarahari MJ, Manshad AK, Ali M, Ali JA, Shafiei A, Sajadi SM, et al. Impact of a novel biosynthesized nanocomposite (SiO2@ Montmorilant@ Xanthan) on wettability shift and interfacial tension: applications for enhanced oil recovery. Fuel 2021;298:120773.
[4] Jackson RB, Le Quéré C, Andrew R, Canadell JG, Korsbakken JI, Liu Z, et al. Global energy growth is outpacing decarbonization. Environ Res Lett 2018;13:120401.
[5] Güney T. Renewable energy, non-renewable energy and sustainable development. Int J Sustain Dev World Ecol 2019;26:389–97.
[6] Arning K, Offermann-van Heek J, Linzenich A, Kätelhön A, Sternberg A, Bardow A, et al. Same or different? Insights on public perception and acceptance of carbon capture and storage or utilization in Germany. Energy Pol 2019;125:235–49.
[7] Bui M, Adjiman CS, Bardow A, Anthony EJ, Boston A, Brown S, et al. Carbon capture and storage (CCS): the way forward. Energy Environ Sci 2018;11:1062–176.
[8] Ali M, Jha NK, Pal N, Keshavarz A, Hoteit H, Sarmadivaleh M. Recent advances in carbon dioxide geological storage, experimental procedures, influencing parameters, and future outlook. Earth Sci Rev 2022;225:103895.
[9] Pal N, Zhang X, Ali M, Mandal A, Hoteit H. Carbon dioxide thickening: a review of technological aspects, advances and challenges for oilfield application. Fuel 2022:122947.
[10] Memon S, Feng R, Ali M, Bhatti MA, Giwelli A, Keshavarz A, et al. Supercritical CO2-Shale interaction induced natural fracture closure: implications for scCO2 hydraulic fracturing in shales. Fuel 2021:122682.
[11] Xu L, Myers M, Li Q, White C, Zhang X. Migration and storage characteristics of supercritical CO2 in anisotropic sandstones with clay interlayers based on X-CT experiments. J Hydrol 2020;580:124239.
[12] Singh K, Anabaraonye BU, Blunt MJ, Crawshaw J. Partial dissolution of carbonate rock grains during reactive CO2-saturated brine injection under reservoir conditions. Adv Water Resour 2018;122:27–36.
[13] Zivar D, Kumar S, Foroozesh J. Underground hydrogen storage: a comprehensive review. Int J Hydrogen Energy 2021;46:23436–62.
[14] Heinemann N, Alcalde J, Miocic JM, Hangx SJ, Kallmeyer J, Ostertag-Henning C, et al. Enabling large-scale hydrogen storage in porous media–the scientific challenges. Energy Environ Sci 2021;14:853–64.
[15] Iglauer S, Akhondzadeh H, Abid H, Paluszny A, Keshavarz A, Ali M, et al. Hydrogen flooding of a coal core: effect on coal swelling. Geophys Res Lett 2022. https://doi.org/10.1029/2021GL096873. e2021GL096873.
[16] Yekta A, Manceau J-C, Gaboreau S, Pichavant M, Audigane P. Determination of hydrogen–water relative permeability and capillary pressure in sandstone: application to underground hydrogen injection in sedimentary formations. Transport Porous Media 2018;122:333–56.
[17] Hashemi L, Blunt M, Hajibeygi H. Pore-scale modelling and sensitivity analyses of hydrogen-brine multiphase flow in geological porous media. Sci Rep 2021;11:1–13.
[18] Yates E, Bischoff A, Beggs M, Jackson N. Hydrogen geo-storage in Aotearoa–New Zealand.
[19] Zhang Y, Zhang Z, Arif M, Lebedev M, Busch A, Sarmadivaleh M, et al. Carbonate rock mechanical response to CO2 flooding evaluated by a combined X-ray computed tomography–DEM method. J Nat Gas Sci Eng 2020;84:103675.
[20] Ni H, Boon M, Garing C, Benson SM. Predicting CO2 residual trapping ability based on experimental petrophysical properties for different sandstone types. Int J Greenh Gas Control 2019;86:158–76.
[21] Dahraj NU, Ali M, Khan MN. End of linear flow time picking in long transient hydraulically fractured wells to correctly estimate the permeability, fracture half-length and original gas in place in liquid rich shales. PAPG/SPE Pakistan section annual technical conference and exhibition. Society of Petroleum Engineers; 2016.
[22] Ali M, Shar AM, Mahesar AA, Al-Yaseri A, Yekeen N, Memon KR, et al. Experimental evaluation of liquid nitrogen fracturing on the development of tight gas carbonate rocks in the Lower Indus Basin, Pakistan. Fuel 2022;309:122192.
[23] Memon KR, Ali M, Awan FUR, Mahesar AA, Abbasi GR, Mohanty US, et al. Influence of cryogenic liquid nitrogen cooling and thermal shocks on petro-physical and morphological characteristics of Eagle Ford shale. J Nat Gas Sci Eng 2021:104313.

[24] Mahesar AA, Ali M, Shar AM, Memon KR, Mohanty US, Akhondzadeh H, et al. Effect of cryogenic liquid nitrogen on the morphological and petrophysical characteristics of tight gas sandstone rocks from kirthar fold belt, Indus Basin, Pakistan. Energy Fuels 2020;34:14548–59.
[25] Yekeen N, Padmanabhan E, Thenesh A, Sevoo L, Kamalarasan A, Kanesen L, et al. Wettability of rock/CO2/brine systems: a critical review of influencing parameters and recent advances. J Ind Eng Chem 2020;88:1–28.
[26] Ali M, Yekeen N, Pal N, Keshavarz A, Iglauer S, Hoteit H. Influence of pressure, temperature and organic surface concentration on hydrogen wettability of caprock; implications for hydrogen geo-storage. Energy Rep 2021;7:5988–96.
[27] Pan B, Yin X, Iglauer S. Rock-fluid interfacial tension at subsurface conditions: implications for H2, CO2 and natural gas geo-storage. Int J Hydrogen Energy 2021;46(50):25578–85.
[28] Ozarslan A. Large-scale hydrogen energy storage in salt caverns. Int J Hydrogen Energy 2012;37:14265–77.
[29] Al-Yaseri A, Abdulelah H, Yekeen N, Ali M, Negash BM, Zhang Y. Assessment of CO2/shale interfacial tension. Colloids Surf A Physicochem Eng Asp 2021;627:127118.
[30] Abdulelah H, Al-Yaseri A, Ali M, Giwelli A, Negash BM, Sarmadivaleh M. CO2/Basalt's interfacial tension and wettability directly from gas density: implications for Carbon Geo-sequestration. J Petrol Sci Eng 2021;204:108683.
[31] Iglauer S, Abid H, Al-Yaseri A, Keshavarz A. Hydrogen adsorption on sub-bituminous coal: implications for hydrogen geo-storage. Geophys Res Lett 2021;48. e2021GL092976.
[32] Tarkowski R. Underground hydrogen storage: characteristics and prospects. Renew Sustain Energy Rev 2019;105:86–94.
[33] Iglauer S, Al-Yaseri AZ, Rezaee R, Lebedev M. CO2 wettability of caprocks: implications for structural storage capacity and containment security. Geophys Res Lett 2015;42:9279–84.
[34] Ali M, Jha NK, Al-Yaseri A, Zhang Y, Iglauer S, Sarmadivaleh M. Hydrogen wettability of quartz substrates exposed to organic acids; Implications for hydrogen trapping/storage in sandstone reservoirs. J Petrol Sci Eng 2021:109081.
[35] Ali M, Aftab A, Arain Z-U-A, Al-Yaseri A, Roshan H, Saeedi A, et al. Influence of organic acid concentration on wettability alteration of cap-rock: implications for CO2 trapping/storage. ACS Appl Mater Interfaces 2020;12:39850–8.
[36] Arif M, Abu-Khamsin SA, Iglauer S. Wettability of rock/CO2/brine and rock/oil/CO2-enriched-brine systems: critical parametric analysis and future outlook. Adv Colloid Interface Sci 2019;268:91–113.
[37] Mutailipu M, Liu Y, Jiang L, Zhang Y. Measurement and estimation of CO2–brine interfacial tension and rock wettability under CO2 sub-and super-critical conditions. J Colloid Interface Sci 2019;534:605–17.
[38] Al-Yaseri A, Ali M, Ali M, Taheri R, Wolff-Boenisch D. Western Australia basalt-CO2-brine wettability at geo-storage conditions. J Colloid Interface Sci 2021;603:165–71.
[39] Hashemi L, Glerum W, Farajzadeh R, Hajibeygi H. Contact angle measurement for hydrogen/brine/sandstone system using captive-bubble method relevant for underground hydrogen storage. Adv Water Resour 2021:103964.
[40] Iglauer S, Ali M, Keshavarz A. Hydrogen wettability of sandstone reservoirs: implications for hydrogen geo-storage. Geophys Res Lett 2021;48. e2020GL090814.
[41] Al-Yaseri A, Jha NK. On hydrogen wettability of basaltic rock. J Petrol Sci Eng 2021;200:108387.
[42] Li D, Neumann A. Equation of state for interfacial tensions of solid-liquid systems. Adv Colloid Interface Sci 1992;39:299–345.
[43] Arif M, Barifcani A, Iglauer S. Solid/CO2 and solid/water interfacial tensions as a function of pressure, temperature, salinity and mineral type: implications for CO2-wettability and CO2 geo-storage. Int J Greenh Gas Control 2016;53:263–73.
[44] Dickson JL, Gupta G, Horozov TS, Binks BP, Johnston KP. Wetting phenomena at the CO2/water/glass interface. Langmuir 2006;22:2161–70.
[45] Ameri A, Kaveh NS, Rudolph E, Wolf KH, Farajzadeh R, Bruining J. Investigation on interfacial interactions among crude oil–brine–sandstone rock–CO2 by contact angle measurements. Energy Fuels 2013;27:1015–25.
[46] Pan B, Gong C, Wang X, Li Y, Iglauer S. The interfacial properties of clay-coated quartz at reservoir conditions. Fuel 2020;262:116461.
[47] Kaveh NS, Barnhoorn A, Wolf K-H. Wettability evaluation of silty shale caprocks for CO2 storage. Int J Greenh Gas Control 2016;49:425–35.
[48] Arif M, Barifcani A, Lebedev M, Iglauer S. Impact of solid surface energy on wettability of CO2-brine-Mineral systems as a function of pressure, temperature and salinity. Energy Proc 2017;114:4832–42.
[49] Ali M, Arif M, Sahito MF, Al-Anssari S, Keshavarz A, Barifcani A, et al. CO2-wettability of sandstones exposed to traces of organic acids: implications for CO2 geo-storage. Int J Greenh Gas Control 2019;83:61–8.
[50] Ali M, Sahito MF, Jha NK, Memon S, Keshavarz A, Iglauer S, et al. Effect of nanofluid on CO2-wettability reversal of sandstone formation; implications for CO2 geo-storage. J Colloid Interface Sci 2020;559:304–12.
[51] Ali M, Awan FUR, Ali M, Al-Yaseri A, Arif M, Sánchez-Román M, et al. Effect of humic acid on CO2-wettability in sandstone formation. J Colloid Interface Sci 2021;588:315–25.
[52] Love JC, Estroff LA, Kriebel JK, Nuzzo RG, Whitesides GM. Self-assembled monolayers of thiolates on metals as a form of nanotechnology. Chem Rev 2005;105:1103–70.
[53] Iglauer S, Salamah A, Sarmadivaleh M, Liu K, Phan C. Contamination of silica surfaces: impact on water–CO2–quartz and glass contact angle measurements. Int J Greenh Gas Control 2014;22:325–8.
[54] Ali M, Al-Anssari S, Arif M, Barifcani A, Sarmadivaleh M, Stalker L, et al. Organic acid concentration thresholds for ageing of carbonate minerals: implications for CO2 trapping/storage. J Colloid Interface Sci 2019;534:88–94.
[55] Al-Anssari S, Barifcani A, Wang S, Maxim L, Iglauer S. Wettability alteration of oil-wet carbonate by silica nanofluid. J Colloid Interface Sci 2016;461:435–42.
[56] Al-Yaseri AZ, Lebedev M, Barifcani A, Iglauer S. Receding and advancing (CO2+ brine+ quartz) contact angles as a function of pressure, temperature, surface roughness, salt type and salinity. J Chem Therm 2016;93:416–23.
[57] Marmur A. Soft contact: measurement and interpretation of contact angles. Soft Matter 2006;2:12–7.
[58] Hosseini M, Fahimpour J, Ali M, Keshavarz A, Iglauer S. Hydrogen wettability of carbonate formations: implications for hydrogen geo-storage. J Colloid Interface Sci 2022;614:256–66.
[59] Ali M, Aftab A, Awan FUR, Akhondzadeh H, Keshavarz A, Saeedi A, et al. CO2-wettability reversal of cap-rock by alumina nanofluid: implications for CO2 geo-storage. Fuel Process Technol 2021;214:106722.
[60] Yekeen N, Padmanabhan E, Idris AK, Chauhan PS. Nanoparticles applications for hydraulic fracturing of unconventional reservoirs: a comprehensive review of recent advances and prospects. J Petrol Sci Eng 2019;178:41–73.
[61] Yekeen N, Manan MA, Idris AK, Padmanabhan E, Junin R, Samin AM, et al. A comprehensive review of experimental

studies of nanoparticles-stabilized foam for enhanced oil recovery. J Petrol Sci Eng 2018;164:43–74.
[62] Dupraz S, Parmentier M, Ménez B, Guyot F. Experimental and numerical modeling of bacterially induced pH increase and calcite precipitation in saline aquifers. Chem Geol 2009;265:44–53.
[63] Yekeen N, Al-Yaseri A, Idris AK, Khan JA. Comparative effect of zirconium oxide (ZrO2) and silicon dioxide (SiO2) nanoparticles on the adsorption properties of surfactant-rock system: equilibrium and thermodynamic analysis. J Petrol Sci Eng 2021;205:108817.
[64] Mohanty US, Awan FUR, Ali M, Aftab A, Keshavarz A, Iglauer S. Physicochemical characterization of zirconia nanoparticle-based sodium alginate polymer suspension for enhanced oil recovery. Energy Fuels 2021;35:19389–98.
[65] Awan FUR, Al-Yaseri A, Akhondzadeh H, Iglauer S, Keshavarz A. Influence of mineralogy and surfactant concentration on zeta potential in intact sandstone at high pressure. J Colloid Interface Sci 2022;607:401–11.
[66] Arif M, Jones F, Barifcani A, Iglauer S. Electrochemical investigation of the effect of temperature, salinity and salt type on brine/mineral interfacial properties. Int J Greenh Gas Control 2017;59:136–47.
[67] Pan B, Yin X, Iglauer S. A review on clay wettability: from experimental investigations to molecular dynamics simulations. Adv Colloid Interface Sci 2020:102266.
[68] Pan B, Yin X, Ju Y, Iglauer S. Underground hydrogen storage: influencing parameters and future outlook. Adv Colloid Interface Sci 2021;294:102473.
[69] Pan B, Li Y, Wang H, Jones F, Iglauer S. CO2 and CH4 wettabilities of organic-rich shale. Energy Fuels 2018;32:1914–22.
[70] Iglauer S, Pentland C, Busch A. CO2 wettability of seal and reservoir rocks and the implications for carbon geo-sequestration. Water Resour Res 2015;51:729–74.
[71] Pan B, Li Y, Xie L, Wang X, He Q, Li Y, et al. Role of fluid density on quartz wettability. J Petrol Sci Eng 2019;172:511–6.
[72] Pan B, Jones F, Huang Z, Yang Y, Li Y, Hejazi SH, et al. Methane (CH4) wettability of clay-coated quartz at reservoir conditions. Energy Fuels 2019;33:788–95.
[73] Al-Yaseri A, Roshan H, Zhang Y, Rahman T, Lebedev M, Barifcani A, et al. Effect of the temperature on CO2/brine/dolomite wettability: hydrophilic versus hydrophobic surfaces. Energy Fuels 2017;31:6329–33.
[74] Iglauer S, Mathew M, Bresme F. Molecular dynamics computations of brine–CO2 interfacial tensions and brine–CO2–quartz contact angles and their effects on structural and residual trapping mechanisms in carbon geo-sequestration. J Colloid Interface Sci 2012;386:405–14.
[75] Arif M, Al-Yaseri AZ, Barifcani A, Lebedev M, Iglauer S. Impact of pressure and temperature on CO2–brine–mica contact angles and CO2–brine interfacial tension: implications for carbon geo-sequestration. J Colloid Interface Sci 2016;462:208–15.
[76] Pan B, Clarkson CR, Atwa M, Debuhr C, Ghanizadeh A, Birss VI. Wetting dynamics of nanoliter water droplets in nanoporous media. J Colloid Interface Sci 2021;589:411–23.
[77] Pan B, Clarkson CR, Atwa M, Tong X, Debuhr C, Ghanizadeh A, et al. Spontaneous imbibition dynamics of liquids in partially-wet nanoporous media: experiment and theory. Transport Porous Media 2021;137:555–74.
[78] Pan B, Yin X, Ju Y, Iglauer S. Underground hydrogen storage: influencing parameters and future outlook. Adv Colloid Interface Sci 2021:102473.
[79] Al-Yaseri AZ, Roshan H, Lebedev M, Barifcani A, Iglauer S. Dependence of quartz wettability on fluid density. Geophys Res Lett 2016;43:3771–6.
[80] Yekeen N, Padmanabhan E, Abdulelah H, Irfan SA, Okunade OA, Khan JA, et al. CO2/brine interfacial tension and rock wettability at reservoir conditions: a critical review of previous studies and case study of black shale from Malaysian formation. J Petrol Sci Eng 2021;196:107673.
[81] Akob DM, Cozzarelli IM, Dunlap DS, Rowan EL, Lorah MM. Organic and inorganic composition and microbiology of produced waters from Pennsylvania shale gas wells. Appl Geochem 2015;60:116–25.
[82] Lundegard PD, Kharaka YK. Distribution and occurrence of organic acids in subsurface waters. Organic acids in geological processes. Springer; 1994. p. 40–69.
[83] Ali M. Effect of organic surface concentration on CO2-wettability of reservoir rock. Curtin University; 2018.
[84] Ali M. Effect of organics and nanoparticles on CO2-wettability of reservoir rock; Implications for CO2 geo-storage. Curtin University; 2021.
[85] Ali M, Yekeen N, Pal N, Keshavarz A, Iglauer S, Hoteit H. Influence of organic molecules on wetting characteristics of mica/H2/brine systems: implications for hydrogen structural trapping capacities. J Colloid Interface Sci 2022;608:1739–49.
[86] Lyklema J. Fundamentals of interface and colloid science: soft colloids. Elsevier; 2005.
[87] Abramov A, Keshavarz A, Iglauer S. Wettability of fully hydroxylated and alkylated (001) α-quartz surface in carbon dioxide atmosphere. J Phys Chem C 2019;123:9027–40.
[88] Arif M, Lebedev M, Barifcani A, Iglauer S. Influence of shale-total organic content on CO2 geo-storage potential. Geophys Res Lett 2017;44:8769–75.
[89] Okunade OA, Yekeen N, Padmanabhan E, Al-Yaseri A, Idris AK, Khan JA. Shale core wettability alteration, foam and emulsion stabilization by surfactant: impact of surfactant concentration, rock surface roughness and nanoparticles. J Petrol Sci Eng 2021;207:109139.
[90] Awan FUR, Keshavarz A, Azhar MR, Akhondzadeh H, Ali M, Al-Yaseri A, et al. Adsorption of nanoparticles on glass bead surface for enhancing proppant performance: a systematic experimental study. J Mol Liq 2021;328:115398.
[91] Al-Anssari S, Arif M, Wang S, Barifcani A, Lebedev M, Iglauer S. Wettability of nanofluid-modified oil-wet calcite at reservoir conditions. Fuel 2018;211:405–14.
[92] Yekeen N, Padmanabhan E, Idris AK. Synergistic effects of nanoparticles and surfactants on n-decane-water interfacial tension and bulk foam stability at high temperature. J Petrol Sci Eng 2019;179:814–30.
[93] Butt H-J, Kappl M. Surface and interfacial forces. John Wiley & Sons; 2018.
[94] Liu TL, Chen Z, Kim C-J. A dynamic Cassie–Baxter model. Soft Matter 2015;11:1589–96.
[95] Al-Khdheeawi EA, Mahdi DS, Ali M, Fauziah CA, Barifcani A. Impact of caprock type on geochemical reactivity and mineral trapping efficiency of CO. Offshore Technology conference Asia. Offshore Technology Conference; 2020.
[96] Jha NK, Al-Yaseri A, Ghasemi M, Al-Bayati D, Lebedev M, Sarmadivaleh M. Pore scale investigation of hydrogen injection in sandstone via X-ray micro-tomography. Int J Hydrogen Energy 2021;46(70):34822–9.
[97] Keshavarz A, Abid H, Ali M, Iglauer S. Hydrogen diffusion in coal: implications for hydrogen geo-storage. J Colloid Interface Sci 2022;608:1457–62.
[98] Jha NK, Lebedev M, Iglauer S, Ali M, Roshan H, Barifcani A, et al. Pore scale investigation of low salinity surfactant nanofluid injection into oil saturated sandstone via X-ray micro-tomography. J Colloid Interface Sci 2020;562:370–80.